Cardiac Motion Analysis Based on Optical Flow on Real-Time Three-Dimensional Ultrasound Data

Qi Duan[a], Elsa D. Angelini[b], Olivier Gerard[c], Kevin D. Costa[a], Jeffrey W. Holmes[a], Shunichi Homma[d], Andrew F. Laine[a]
[a]Department of Biomedical Engineering, Columbia University, ET351, 1210 Amsterdam Avenue, New York, NY, USA, 10027
[b]Ecole Nationale Supérieure des Télécommunications, Département Traitement du Signal et des Images (TSI), 46 rue Barrault, Paris, France, 75013
[c]Philips France, 51 rue Carnot, BP 301, Suresnes, France, 92156
[d]Department of Medicine, Columbia University,
Cardiology Division, Ph 9 East 111, 622 W 168 street, 10032, New York, NY, USA

ABSTRACT

With relatively high frame rates and the ability to acquire volume data sets with a stationary transducer, 3D ultrasound systems, based on matrix phased array transducers, provide valuable three-dimensional information, from which quantitative measures of cardiac function can be extracted. Such analyses require segmentation and visual tracking of the left ventricular endocardial border. Due to the large size of the volumetric data sets, manual tracing of the endocardial border is tedious and impractical for clinical applications. Therefore the development of automatic methods for tracking three-dimensional endocardial motion is essential. In this study, we evaluate a four-dimensional optical flow motion tracking algorithm to determine its capability to follow the endocardial border in three dimensional ultrasound data through time. The four-dimensional optical flow method was implemented using three-dimensional correlation. We tested the algorithm on an experimental open-chest dog data set and a clinical data set acquired with a Philips' iE33 three-dimensional ultrasound machine. Initialized with left ventricular endocardial data points obtained from manual tracing at end-diastole, the algorithm automatically tracked these points frame by frame through the whole cardiac cycle. Finite element surfaces were fitted through the data points obtained by both optical flow tracking and manual tracing by an experienced observer for quantitative comparison of the results. Parameterization of the finite element surfaces was performed and maps displaying relative differences between the manual and semi-automatic methods were compared. The results showed good consistency with less than 10% difference between manual tracing and optical flow estimation on 73% of the entire surface. In addition, the optical flow motion tracking algorithm greatly reduced processing time (about 94% reduction compared to human involvement per cardiac cycle) for analyzing cardiac function in three-dimensional ultrasound data sets. A displacement field was computed from the optical flow output, and a framework for computation of dynamic cardiac information is introduced. The method was applied to a clinical data set from a heart transplant patient and dynamic measurements agreed with known physiology as well as experimental results.

To be appear in:

Recent Advances in Diagnostic and Therapeutic Ultrasound Imaging for Medical Applications, Suri *et al* Eds., Artech House Press 2006 (in press).

Chapter 9

Cardiac Motion Analysis Based on Optical Flow on Real-Time 3D Ultrasound Data

With relatively high frame rates and the ability to acquire volume data sets with a stationary transducer, 3D ultrasound systems, based on matrix phased array transducers, provide valuable three-dimensional information, from which quantitative measures of cardiac function can be extracted. Such analyses require segmentation and visual tracking of the myocardial borders. Due to the large size of the volumetric data sets, manual tracing of the endocardial border is tedious and impractical for clinical applications. In addition, manual tracing usually requires slicing the 3D data set into 2D images which loses some of the spatial continuity and makes manual boundary detection more error-prone. Therefore the development of automatic methods for tracking three-dimensional endocardial motion is essential. In this study, we evaluate a four-dimensional optical flow motion tracking algorithm to determine its capability to follow the left ventricular borders in three dimensional ultrasound data through time. The optical flow method was implemented using three-dimensional correlation. We tested the algorithm on an experimental open-chest dog data set and a clinical data set both acquired with a Philips' iE33 three-dimensional ultrasound machine. Initialized with left ventricular endocardial data points obtained from manual tracing at end-diastole, the algorithm automatically tracked these points frame by frame through the whole cardiac cycle. A finite element surface was fitted through the data points obtained by both optical flow tracking and manual tracing from an experienced observer for quantitative comparison of the results. Parameterization of the finite element surfaces was performed and maps displaying relative differences between the manual and semi-automatic methods were compared. The results showed good consistency between manual

tracing and optical flow estimation on 73% of the entire surface with fewer than 10% difference. In addition, the optical flow motion tracking algorithm greatly reduced processing time (about 94% reduction compared to human involvement per cardiac cycle) for analyzing cardiac function in three-dimensional ultrasound data sets. A displacement field was computed from the optical flow output, and a framework for computation of dynamic cardiac information was introduced. The method was applied to a clinical data set from a heart transplant patient and dynamic measurements agreed with physiological knowledge as well as experimental results.

9.1 REAL-TIME 3D ECHOCARDIOGRAPHY

Developments in three-dimensional echocardiography started in the late 1980s with the introduction of off-line three-dimensional medical ultrasound imaging systems. The evolution of three-dimensional ultrasound acquisition systems can be divided into three generations: freehand scanning, mechanical scanning and matrix-phased arrays. Many review articles have been published over the past decade, assessing the progress and limitations of three-dimensional ultrasound technology for clinical screening [1-10].

Development of real-time 3D (RT3D) echocardiography started in the late 1990s by Volumetrics [11] based on matrix phased arrays transducers. Recently, a new generation of RT3D transducers was introduced by Philips Medical Systems (Best, The Netherlands) with the SONOS 7500 transducer followed by the iE33 that can acquire a fully sampled cardiac volume in four cardiac cycles. This technical design enabled a dramatic increase in spatial resolution and image quality, which makes such 3D ultrasound techniques increasingly attractive for daily cardiac clinical diagnoses. Since RT3D ultrasound acquires volumetric ultrasound sequences with fairly high temporal resolution and a stationary transducer, it can capture the complex 3D cardiac motion very well.

Advantages of using three-dimensional ultrasound in cardiology include the possibility to display a three-dimensional dynamic view of the beating heart, and the ability for the cardiologist

to explore the three-dimensional anatomy at arbitrary angles, to localize abnormal structures and assess wall motion. This technology has been shown, in the past decade, to provide more accurate and reproducible screening for quantification of cardiac function for two main reasons: the elimination of assumptions about ventricular geometry and the improved selection of the visualization planes for performing the ventricular volume measurements. It was validated through several clinical studies for quantification of LV function as reviewed in [12]. Nevertheless, full exploitation of three-dimensional ultrasound data for qualitative and quantitative evaluation of cardiac function remains sub-optimal for two reasons: lack of appropriate display and lack of automatic boundary detection. Manual tracing of myocardial borders is a tedious task that requires the intervention of an expert cardiologist familiar with the ultrasound machine. Also slicing the 3D data set into 2D images loses some of the spatial continuity and makes manual boundary detection more error-prone. For this reason, ventricular volumes are commonly estimated via visual inspection of two-dimensional B-scan images or semi-automated segmentation for difficult cases. Existing commercialized semi-automatic segmentation programs include TomTec by TomTec Inc (Munich, Germany) and QLAB by Philips (Best, The Netherlands).

9.2 ANISOTROPIC DIFFUSION

The presence of speckle noise patterns makes the interpretation of ultrasound images, either by a human operator or with a computer-based system, very difficult. It is highly desirable for certain applications such as automatic segmentation, to apply some denoising prior to scan conversion in order to remove speckle noise artifacts and improve signal homogeneity within distinct anatomical tissues. A number of methods have been proposed to de-noise and improve the ultrasound image quality including temporal averaging, median filtering, maximum amplitude writing (temporal dilation), adaptive speckle reduction (ASR) (statistical enhancement) [13-17], adaptive weighted median filter (AWMF) [18], homomorphic Wiener filtering, and wavelet

shrinkage (WS) [19, 20]. Most of these methods suffer from either insufficient denoising, image quality degradation or large computational cost. Furthermore, some of them require raw "radio-frequency" data, available prior to logarithmic compression [21]. Our group has presented previous work on applying brushlet denoising in spherical coordinates to RT3D cardiac ultrasound [22]. Experiments on phantom and clinical cardiac data sets have shown excellent performance of the method. However, the main limitation of this type of denoising remains the computational cost that prevents for the moment its implementation for real-time visualization applications in clinical practice.

In this context, in [23], we have investigated the performance of a more computationally efficient denoising filter based on anisotropic diffusion for data represented in spherical coordinates. A similar framework can be found in the work of Abd-Elmoniem *et al.*[21, 24] who used two-dimensional anisotropic filtering in radial coordinates. Anisotropic diffusion methods are very efficient for speckle reduction in ultrasound and radar images. Yu and Acton [25, 26] applied their speckle reducing filter on synthetic aperture radar images and compared their performance to Lee and Kuan filters and Frost filters. These filters are all derived from anisotropic diffusion. Finally Montagnat *et al* applied a three-dimensional anisotropic diffusion filter for rotational cardiac 3D ultrasound data [27].

Anisotropic diffusion methods apply the following heat-diffusion type of dynamic equation to the gray levels of a given 3D image data $I(x,y,z,t)$:

$$\frac{\partial I}{\partial t} = div(c(x,y,z,t)\nabla I) \tag{9.1}$$

where $c(x,y,z,t)$ is the diffusion parameter, *div* denotes the divergence operator, and ∇I denotes the gradient of the image intensity. In the original work of Perona and Malik [28, 29], the concept of anisotropic diffusion was introduced with the selection of a variable diffusion parameter, as a function of the gradient of the data:

$$c(x,y,z,t) = g\left(\left|\nabla I(x,y,z,t)\right|\right) \tag{9.2}$$

We used the diffusion function proposed by Weickert [30] defined as:

$$g(x,\lambda)=\begin{cases}1 & x\le 0\\ 1-e^{-\frac{3.315}{(x/\lambda)^4}} & x>0\end{cases} \tag{9.3}$$

The parameter λ serves as a gradient threshold, defining edge points x_k as locations where $\left|\nabla I_{x_k}\right|>\lambda$. This bell-shaped diffusion function acts as an edge-enhancing filter, with high diffusion values in smooth areas and low values at edge points. The structure of the diffusion tensor with separate weights for each dimension enables it to control the direction of the diffusion process, with flows parallel to edge contours.

In the case of ultrasound, as the diffusion process evolves, image data properties change dramatically and it is desirable to modify the gradient threshold parameter value. In their paper, Montagnat *et al*. report a decrease in the value of significant edges as the homogeneous regions in the ultrasound data are filtered. They therefore chose to decrease the threshold gradient in time and proposed values based on a fraction of the cumulative histograms of the data gradients recomputed at each iteration of the diffusion process. In our case, we used a linear model in [23] where:

$$\lambda(t)=\lambda_0+a\,t \tag{9.4}$$

with λ_0 an initial gradient value, a is a slope parameter and t is the time iteration index. Parameters were set empirically for the data sets processed. Specifically in [23], we chose an increasing threshold in order to smooth out sampling artifacts as well as remove speckle noise.

Filtering performance was assessed in terms of visual quality and for quantitative measurements on a phantom object in [23]. Our quantitative study showed that very high measurement accuracy could be achieved but required suitable parameter settings of the scan conversion method, while visual quality was similar for all interpolation kernels.

9.3 TRACKING OF LV ENDOCARDIAL SURFACE ON REAL-TIME THREE-DIMENSIONAL ULTRASOUND WITH OPTICAL FLOW

Clinical evaluation of 3D ultrasound data for assessment of cardiac function is performed via interactive inspection of animated data, along selected projection planes. Facing the difficulty of inspecting a 3D data set with 2D visualization tools, it is highly desirable to assist the cardiologist with quantitative tools for analysis of 3D ventricular function. Complex and abnormal ventricular wall motion, for example, can be detected, at a high frame rate, via quantitative four-dimensional analysis of the endocardial surface and computation of local fractional shortening [31]. Such preliminary studies showed that RT3D ultrasound provides unique and valuable quantitative information about cardiac motion, when derived from manually traced endocardial contours. Recent software tools provide interactive segmentation capabilities for the endocardium using a 3D deformable model that alleviates the need for full manual tracing of the endocardial border. To assist the segmentation process over the entire cardiac cycle, we evaluated the use of optical flow (OF) tracking between segmented frames and tried to answer the following questions in [32]: *Can OF track the endocardial surface between ED and ES with reliable positioning accuracy? How does dynamic information derived from OF tracking on RT3D ultrasound compare to manual tracing method, given the high inter and intra variability of segmentation by experts? Can OF be used as a dynamic interpolation tool for tracking the endocardial surface?*

Cardiac motion analysis from images has been an active research area over the past decade. However, most research efforts were based on CT and MRI data. Previous efforts using ultrasound data for motion analysis include intensity-based OF tracking, strain-imaging, and elastography. Intensity-based OF tracking methods described in [33-38] combine local intensity correlation with specific regularizing constraints (e.g. continuity). For strain-imaging or elastography, strain calculation and motion estimation are typically derived from auto-correlation and cross-correlation on RF data. The commercialized strain imaging package, “2D Strain” from

General Electric [39] uses such a paradigm. Most published papers on strain-imaging or elastography [39-43] are limited to 1D or 2D images. Early studies [44] used simple simulated phantoms while recent research [45] used 3D ultrasound data sequence for LV volume estimation. The presence of speckle noise in ultrasound prevents the use of gradient-based methods while relatively large region-matching methods are reasonably robust to the presence of noise. In this study, we propose a surface tracking technique based on a 4D correlation-based OF method on 3D volumetric ultrasound intensity data.

9.3.1 Correlation-based Optical Flow

Optical flow tracking refers to the computation of the displacement field of objects in an image, based on the assumption that the intensity of the object remains constant. In this context, motion of the object is characterized by a flow of pixels with constant intensity. The assumption of intensity conservation is typically unrealistic for natural movies and medical imaging applications, motivating the argument that OF can only provide *qualitative* estimation of object motions. There are two global families of OF computation techniques: (1) Differential techniques [46-48] that compute velocity from spatio-temporal derivatives of pixel intensities; (2) Region-based matching techniques [49, 50], which compute OF via identification of local displacements that provide optimal homogeneity measure between two consecutive image frames. Compared to differential OF approaches, region-based methods using homogeneity measures are less sensitive to noisy conditions and fast motion [51] but assume that displacements in small neighborhoods are similar. For three-dimensional ultrasound, this latter approach appeared more appropriate and was selected for this study. Given two data sets from consecutive time frames: $\left(I(\mathbf{x},t), I(\mathbf{x},t+\Delta t)\right)$, the displacement vector $\Delta\mathbf{x}$ for each pixel in a small neighborhood Ω around a pixel x is estimated via maximization of the cross-correlation coefficient defined as:

$$r = \frac{\sum_{\mathbf{x}\in\Omega}\left(I(\mathbf{x},t)I(\mathbf{x}+\Delta\mathbf{x},t+\Delta t)\right)}{\sqrt{\sum_{\mathbf{x}\in\Omega} I^2(\mathbf{x},t)\sum_{\mathbf{x}\in\Omega} I^2(\mathbf{x}+\Delta\mathbf{x},t+\Delta t)}} \tag{9.5}$$

In [32], correlation-based OF was applied to estimate the displacement of selected voxels between two consecutive ultrasound volumes in the cardiac cycle. The search window Ω was centered about every (5×5×5) pixel volume and was set to size (7×7×7). To increase the robustness of the estimation, the final estimation of the displacement for each point is the average within a 6-connected neighborhood.

9.3.2 Three-Dimensional Ultrasound Data Sets

The tracking approach was tested on three data sets acquired with a SONOS 7500 3D ultrasound machine (Philips Medical Systems, Best, The Netherlands):

(1) Two data sets on an anesthetized open chest dog were acquired before (baseline) and 2 minutes after induction of ischemia via occlusion of the proximal left anterior descending coronary artery. These data sets were obtained by positioning the transducer directly on the apex of the heart, providing high image quality and a small field of view. Spatial resolution of the analyzed data was ($0.56mm^3$) and 16 frames were acquired per cardiac cycle.

(2) One transthoracic clinical data set was aquired from a heart-transplant patient. Spatial resolution of the analyzed data was ($0.8mm^3$) and 16 frames were acquired for one cardiac cycle. Because of the smaller field of view used to acquire the open-chest dog data and the positioning of the transducer directly on the dog's heart, image quality was significantly higher in this data set, with some fine anatomical structures visible. Cross-section views at end-diastole (ED) from the open-chest baseline data set, and the patient data set are shown in Figure 9.1.

Figure 9.1 *Cross-sectional views at ED for (a-c) Open-chest dog data, prior to ischemia, (d-f) Patient with transplanted heart. (a, d) axial, (b, e) elevation and (c, f) azimuth views.*

9.3.3 Surface Tracing

The endocardial surface of the left ventricle (LV) was extracted with two methods. (1) An expert performed manual tracing of all time frames in the data sets, on rotating B-scan views (long-axis views rotating around the central axis of the ventricle) and C-scan views (short-axis views at different depths). (2) The QLAB software, (Philips Medical Systems), was used to segment the endocardial surface. Initialization was performed by a human expert and a parametric deformable model was fit to the data at each time frame. Segmentation results were reviewed by the same expert and adjusted manually for final corrections. We emphasize here that QLAB is used as a semi-automated segmentation tool. The QLAB software was designed to process human clinical data sets. Because significant anatomical differences between canine and human hearts could lead to misbehavior of the segmentation software, we decided to only apply the software tool to clinical data sets.

9.3.4 Surface Tracking with Optical Flow

Tracking of the endocardial surface with OF was applied after initialization using the manually traced surfaces (for dog data and clinical data) and the QLAB segmented surfaces (for clinical data). Starting with a set of endocardial surface points (about three thousand points, roughly 1 mm apart for manual tracing and about eight hundred points, roughly 3 mm apart for QLAB) defined at end-diastole, the OF algorithm was used to *track the surface in time through the whole cardiac cycle*. Since the correlation-based OF method is very sensitive to speckle noise, all data sets were pre-smoothed with edge-preserving anisotropic diffusion as developed in [23] and described above (§9.2). We emphasize here that OF was not applied as a segmentation tool but as a surface tracking tool for a given segmentation method.

9.3.5 Evaluation

We evaluated OF tracking performance via visualization and quantification of dynamic ventricular geometry compared to segmented surfaces. Usually comparison of segmentation

results is performed via global measurements like volume difference or mean-squared error. In order to provide local comparison, we proposed a novel comparison method in [52] based on a parameterization of the endocardial surface in prolate spheroidal coordinates [53] and previously used for comparison of ventricular geometries from two 3D ultrasound machines in [54]. The endocardial surfaces were registered using three manually selected anatomical landmarks: the center of the mitral orifice, the endocardial apex, and the equatorial mid-septum. The data were fitted in prolate spheroidal coordinates (λ, μ, θ), projecting the radial coordinate λ to a 64-element surface mesh with bicubic Hermite interpolation, yielding a realistic 3D endocardial surface. The fitting process (illustrated in Figure 9.2 for a single endocardial surface) was performed using custom routines written in MATLAB. In this figure, we can observe the initial positioning of the data points and the surface mesh, and the finite element surface after fitting with very high agreement between the data and the mesh. A zoom is provided on a small region, showing the quality of agreement between the fitted surface and the points resulting from region-based global optimization of radial projections.

The fitted nodal values and spatial derivatives of the radial coordinate, λ, were then used to map relative differences between two surfaces, $\varepsilon = (\lambda_{seg} - \lambda_{OF}) / \lambda_{seg}$ using custom software. A Hammer mapping was used to flatten the endocardial surface via an area preserving mapping [55]. For each time frame, root mean squared errors (RMSE) of the difference in λ, summed over all nodes on the endocardial surface, were computed between OF and individual segmentation methods. Ventricular volumes were also computed from the segmented and the tracked endocardial surfaces. Finally relative λ difference maps were generated for end-systole (ES), providing a direct quantitative comparison of ventricular geometry. These maps are visualized with iso-level lines, quantified in fractional values of radial difference.

Figure 9.2 *Fitting process of the endocardial surface at ES. (a) Initial FEM mesh and data points. (b) Fitted FEM surface and data points. (c) Zoom on a small region with the FEM fitted surface and the data points.*

9.3.6 Results

Figure 9.3 *Endocardial surfaces from open-chest dog data sets at ES. (a-c) Results on baseline data. (d-f) Results on post-ischemia data. Three-dimensional rendering of endocardial surfaces were generated from manual tracing (dark gray) and OF tracking (light gray) for (a, d) lateral views and (b, e) anterior views. (c, f) Relative difference maps between OF and manual tracing surfaces.*

9.3.6.1 Dog Data

On the dog data sets, RMSE results reported a maximum radial absolute difference of 0.19 (average radial coordinate value was 0.7±0.2 at ED and 0.6±0.3 at ES) at frame 11 (start of diastole) on the baseline data set and 0.08 (average radial coordinate value was 0.7±0.3 at ED and 0.6±0.2 at ES) at frame 12 (start of diastole) on the post-ischemia data set. Maximum LV volume differences were less than 7 ml on baseline data and 5ml on the post-ischemia data set. RMSE values were smaller for OF tracking on larger volumes. On the radial difference maps in Figure 9.3, we observe similar difference patterns in the baseline and the post-infarct data except for a dark region near the apical lateral region, demonstrating repeatability of the OF tracking performance on a given ventricular geometry but with different contractility patterns. An area with large error in the baseline comparison localized on the anterior-lateral wall disappeared in post-ischemia tracking. This error is caused by a small portion of tracked points that were confused by acquisition artifacts at the boundary between the first and second quadrants of acquisition. Errors were rather evenly distributed over the endocardial surface with overall shape agreement. Similar maps can be used to examine local fractional shortening using the technique developed by the Cardiac Biomechanics Group at Columbia University [55] and revealed similar patterns of abnormal wall motion after ischemia using OF tracked surface or manual tracing, corroborating the accuracy of OF tracking to provide dynamic functional information.

9.3.6.2 Clinical Data

OF tracking was run with initialized surfaces provided by either manual tracing or the QLAB segmentation tool on the clinical data set. Because of lower image quality on the clinical data set,

compared to the open-chest dog data, we performed two sets of additional experiments. First, we checked if the time frame selected for initialization had an influence on the tracking quality.

Figure 9.4 *Clinical Data: (a) RMSE between OF tracking and manual tracing: forward (solid line) and backward (dashed line). (b) RMSE between OF tracking and QLAB segmentation: forward tracking without re-initialization (solid line), forward tracking with re-initialization every fourth frame (dashed line), forward tracking with re-initialization every second frame (dotted line), and average result from forward and backward tracking without re-initialization (dashdot line).*

Based on manual tracing, we initialized OF tracking for the whole cardiac cycle with ED (forward tracking) or ES (backward tracking) and compared RMSE over the entire cycle. Results, plotted in Figure 9.4a show very comparable performance, confirming that the OF seems to be repeatable and insensitive to initialization set up. We therefore selected the first volume in the sequences, which always corresponds to ED in our experiments. A second experiment evaluated the agreement between QLAB and OF tracking when increasing the number of reference surfaces used to re-initialize OF over the cardiac cycle. Results, plotted in Figure 9.4b, show that agreement of OF tracking and QLAB segmentation increases with re-initialization frequency and reaches RMSE levels similar to the experiment with manual tracing for re-initialization (i.e. reload QLAB segmentation for that frame instead of using the tracing result from previous frame) every other frame. We point out that strong smoothing constraints, applied by the deformable model of the QLAB segmentation, lead to surface positioning that did not always correspond to the apparent high contrast interface. Finally, we compared RMSE values from forward tracking and from averaging forward and backward tracked shapes. We observed a large increase in agreement with the QLAB smooth segmentation when averaging tracked surfaces.

As shown in Figure 9.5, experiments showed that OF tracking initialized with manual tracing provides ventricular endocardial surfaces similar to that obtained by manual tracing, with less than 0.1 maximum absolute differences in RMSE and maximum LV volume differences below 10 ml. When initialized with QLAB, OF tracking with re-initialization shows results with less than 0.08 maximum RMSE difference and less than 13 ml for LV volume differences. These

differences are similar to inter and intra-observer variability for measurement of LV volume by echocardiography [56, 57].

Figure 9.5 *Results on clinical data. (a) RMSE of radial difference for OF initialized with manual tracing (solid line) and QLAB segmentation with 2-frame re-initialization (dashed line); (b-c) LV volumes over one cardiac cycle: (b) Manual tracing (solid line) and OF initialized with manual tracing (dashed line); (c) QLAB segmentation (solid line) and OF initialized with QLAB segmentation (dashed line).*

Ventricular geometries are illustrated in Figure 9.6. We again observed high overall agreement between endocardial geometries provided by manual tracing and OF tracking. Radial differences were distributed over the entire surface, with higher values on the lateral-posterior wall. The QLAB segmentation provided very smooth surfaces, well tracked by the OF. Larger errors were again observed on the lateral posterior wall. Comparison of the two experiments shows that OF over one time-frame can preserve the smoothness of the surface but will tend towards more convoluted surfaces during temporal propagation of the tracking process.

Figure 9.6 *Endocardial surfaces from clinical data at ES. (a-c) Manual tracing; (d-f) QLAB segmentation. Three-dimensional rendering of endocardial surfaces from segmentation method (dark gray) and OF tracking (light gray): (a, d) lateral view; (b, e) anterior view. Relative radial difference maps between OF tracking and the segmentation method.*

The time needed for computing optical flow is about 30 seconds per frame, comparing with 5-10 minutes per frame with manual tracing. With optical flow, the processing time for model-based 3D cardiac motion analysis can be cut from 30-60 minutes to 3 minutes, which makes the application of 3D cardiac motion analysis much more practicable in clinical applications.

Based on the high agreement with manual tracing, we can infer that OF might be a good candidate method to guide a deformable model with high smoothness constraints to better adapt to the ultrasound data and incorporate temporal information in the segmentation process. On the other hand, OF tracking could be adapted to these smoothness constraints, better ranked by cardiologists, to track larger spatial windows around the endocardial surface.

9.4 DYNAMIC CARDIAC INFORMATION FROM OPTICAL FLOW

In [58], we extended our approach to the extraction of motion fields, generated from the optical flow algorithm that efficiently described complex 3D myocardial deformations. Traditional approaches convert displacement information recovered from the image data in Cartesian coordinates into polar (2D) or cylindrical (3D) coordinates to adapt to the natural shape of the left ventricle. Most efforts to quantify cardiac motion from echocardiography focus on radial and circumferential displacements, but ignore gradients of displacements, like thickening and twist. These gradients are of great diagnostic interest and are critical for biomechanical modeling. In this context, we proposed a framework based on semi-automatic four-dimensional optical flow to compute important dynamic cardiac information using RT3D ultrasound.

In this study, optical flow algorithm sequentially estimated the displacement field between two consecutive frames throughout the ejection phase from ED to ES on the clinical data set in previous section. Myocardial motion is estimated via optical flow tracking using a similar scheme in [32]. Cardiac dynamic measurements (displacements and their derivatives) are then computed. A flowchart of the computational framework is provided in Figure 9.7.

Figure 9.7 *Flowchart of the computational framework.*

9.4.1 Coordinate Systems

Three coordinate systems are involved in the computational framework (see Figure 9.8): pixel coordinates *(i, j, k)*, Cartesian coordinates *(x, y, z),* and cylindrical coordinates *(r, θ, z)*. The OF estimation was performed in pixel coordinates. For computation of dynamic information, displacements in pixel coordinates were converted into Cartesian coordinates and centered inside the ventricular cavity so that the z-axis is aligned with the long axis of left ventricle. This coordinate transform is performed via rigid transformation:

$$\begin{bmatrix} x \\ y \\ z \end{bmatrix} = R \begin{bmatrix} i \\ j \\ k \end{bmatrix} + T = \begin{bmatrix} r_{11} & r_{12} & r_{13} \\ r_{21} & r_{22} & r_{23} \\ r_{31} & r_{32} & r_{33} \end{bmatrix} \begin{bmatrix} i \\ j \\ k \end{bmatrix} + \begin{bmatrix} -O_i \\ -O_j \\ -O_k \end{bmatrix} \tag{9.6}$$

where R is a rotation matrix, T is a translation vector, equal to the negative pixel coordinates of the origin O of the Cartesian coordinate system. The ventricular axis was defined as the axis connecting the center of the mitral orifice and the endocardial apex. This axis has a very stable position during the whole cardiac cycle [55]. Based on the Cartesian coordinate system, a corresponding cylindrical coordinate system is established with the r-θ plane corresponding to the x-y plane and with the x-axis used as the reference for θ.

Figure 9.8 *Coordinate systems for data acquisition, and computation.*

9.4.2 Dynamic Cardiac Information Measurements

Besides displacement (u_x, u_y, u_z) in Cartesian coordinates, we computed the following dynamic measurements:

- Flow magnitude $|u|$ (mm)
- Radial displacement u_r (mm)
- Circumferential displacement u_θ (mm)
- Thickening $\partial u_r / \partial r$
- Circumferential stretch $\partial u_\theta / \partial \theta$
- Longitudinal stretch $\partial u_z / \partial z$
- Twist $\partial u_\theta / \partial z$

Gradient values were computed directly in pixel coordinates and converted into the cylindrical coordinate system via the chain rule. Derivatives in pixel coordinates were approximated by central difference operators to accommodate second-order continuity of the flow field after RBF Interpolation.

9.4.3 Data

We used the heart transplant clinical data set described in the previous section. Due to the heart-transplant surgery procedure, the patient had reduced cardiac function and his septum had significant motion reduction. Due to field of view limitations, the apical epicardial surface was not visible in the ultrasound volume. Therefore only the basal and middle parts of left ventricle were used for dynamic analysis. In fact, myocardial shape in this region can be well approximated by a cylinder, which can reduce geometric errors in radial displacement estimation.

9.4.4 Results and Discussion

We present results for computation of myocardial flow field (Figure 9.9), radial displacement (Figure 9.10), thickening (Figure 9.11), and twist (Figure 9.12) during the systolic phase.

Most of the radial displacement components showed inward motion (negative displacement) of the ventricular wall, except on the septal side, where reduced amplitude and outward motion was observed (Figure 9.10). These findings were in agreement with clinical observations on the dataset and typical findings after heart-transplant surgery. The gradient of radial displacement, or thickening, yielded positive thickening at the endocardial surface except for the septal wall where zero or small thinning at the epicardium border were observed (Figure 9.11). Such a pattern agrees with experimental findings [60, 61]. Regarding twist, most parts of the wall exhibited clockwise twist patterns relative to the base, when looking from base to apex. This result also agrees with experimental findings [60, 61] of positive (clockwise) twist during the systolic phase. However, we observed negative twist values in the septal wall. For most parts of the wall, twist values increased radially from the epicardial to the endocardial surface, which concurs with theoretical and experimental results [61].

Figure 9.9 *Flow field: (a) 1 slice; (b) 3D rendering.*

Figure 9.10 *Radial displacement: (a) 1 slice (blue: inward); (b) 3D rendering*

Figure 9.11 *Thickening: (a) 1 slice; (b) 3D rendering.*

Figure 9.12 *Twist: (a) 1 slice (blue: clockwise); (b) 3D rendering*

9.4.5 Discussion on Estimation of Myocardial Field

Different schemes exist to estimate the myocardial motion field using optical flow in real-time 3D echocardiography. In [62], four different optical flow based schemes, including the one proposed in [58], were investigated under a generalized framework.

Scheme 1: Boundary tracking with RBF interpolation [59], as we proposed in [58].

Scheme 2: Direct tracking within a myocardial mask. A straightforward alternative to scheme 1 is to track with OF every voxel within a myocardial mask defined by the myocardial surfaces, instead of interpolating the OF tracking result of these surfaces.

Scheme 3: Full-field OF estimation. A more global approach consists of estimating the motion field for all the voxels in the input volumes using OF. The myocardial motion field is then extracted by masking the motion field of the voxels belonging to the myocardium.

Scheme 4: Full-field OF estimation with smoothing. The RBF interpolation of scheme 1 provided a 2^{nd}-order continuity which is not used in direct OF estimation. We tested an alternative to Scheme 3 by adding smoothing via cubic spline regularization on the full field OF computation.

The experiment results showed that:

The radial displacement fields derived from the four different schemes were similar except for fine details within the myocardium. This is expected since all the methods depended on the OF tracking results. For the radial thickening, Scheme 1, 3, and 4 provided similar results as well whereas Scheme 2 produced flawed results due to the derivative calculation across the boundary.

The thickening values of the normal part of the wall from Schemes 1, 3, and 4 (around 0.1~0.25) were close to the normal values reported in [63] (0.1~0.4) and [64] (20-40%) .

The segmental averaged thickening result showed that anterior and lateral segments had normal motion whereas the septal segment had outward motion and negative thickening (i.e. thinning) values; the posterior and anteroseptal segments had reduced motion; the inferior segments had very small deformation or thickening.

All schemes required the same amount of manual initialization, i.e. endo- and epicardial tracing at ED. In terms of accuracy, Scheme 3 was more accurate in displacement estimation; however, Scheme 4 was more robust in estimating thickening, benefited from its intrinsic smoothness constraints.

One important thing needed to be pointed out is that although on some "normal" data sets, the interpolated scheme (scheme 1) and the full field schemes (schemes 3, 4) may have similar results, we still recommend using a full field scheme, e.g. scheme 4 or more sophisticated field fitting techniques, for myocardial deformation estimation instead of using an interpolated version from the ventricular boundary, in order to capture the abnormal motion patterns within the myocardium. Interpolated scheme should not been used in clinical settings.

9.5 SUMMARY

Real-time three-dimensional echocardiography (RT3DE) provides valuable three-dimensional information, from which quantitative measures of cardiac function can be extracted. In this chapter, we proposed an optical-flow based method to extract the ventricular boundaries semi-automatically and validated on experimental and clinical data sets. Information extracted by optical flow can be fed into model-based motion analysis tools. With huge saving in processing time, optical flow makes such cardiac motion analysis on RT3DE more practicable in clinical applications. Myocardial motion field can also be estimated based on the optical flow estimation, from which clinical meaningful cardiac dynamic metrics can be derived.

9.6 ACKNOWLEDGEMENTS

This work was funded by National Science Foundation grant BES-02-01617, American Heart Association #0151250T, Philips Medical Systems, New York State NYSTAR/CAT Technology Program, and the Louis Morin Fellowship program. The authors also would like to thank Dr.

Todd Pulerwitz (Department of Medicine, Columbia University), Susan L. Herz, and Christopher M. Ingrassia.

References

[1] E. O. Ofili and N. C. Nanda, "Three-dimensional and four-dimensional echocardiography," *Ultrasound Medical Biology*, vol. 20, 1994.
[2] A. Fenster and D. B. Downey, "Three-Dimensional Ultrasound Imaging," in *Handbook of Medical Imaging Volume1 Physics and Psychophysics*, vol. 1, H. L. K. Jacob Beutel, Richard L. Metter, Ed. Bellingham, WA, USA.: SPIE- The International Society of Optical Engineering, 2000, pp. 463-510.
[3] R. N. Rankin, A. Fenster, D. B. Downey, P. L. Munk, M. F. Levin, and A. D. Vellet, "Three-dimensional sonographic reconstruction: technique and diagnostic applications," *American Journal of Radiology*, vol. 161, pp. 695-702, 1993.
[4] M. Belohlavek, D. A. Foley, T. C. Gerber, T. M. Kinter, J. F. Greenleaf, and J. B. Seward, " ultrasound imaging: a new era for echocardiography," *Mayo Clinic Proceedings*, vol. 68, pp. 221-240, 1993.
[5] J. R. Warmath, P. Bao, A. J. Herline, and R. L. Galloway, "Ultrasound 3D volume reconstruction from an optically tracked endorectal ultrasound (TERUS) probe," San Diego, CA, United States, 2004.
[6] R. Managuli, E.-H. Kim, K. Karadayi, and Y. Kim, "Advanced volume rendering algorithm for real-time 3D ultrasound: Integrating pre-integration into shear-image-order algorithm," San Diego, CA, United States, 2006.
[7] H. Zhang, F. Banovac, A. White, and K. Cleary, "Freehand 3D ultrasound calibration using an electromagnetically tracked needle," San Diego, CA, United States, 2006.
[8] H. Yu, M. S. Pattichis, and M. Beth Goens, "Multi-view 3D reconstruction with volumetric registration in a freehand ultrasound imaging system," San Diego, CA, United States, 2006.
[9] J. Sanches, J. M. Bioucas-Dias, and J. S. Marques, "Minimum total variation in 3D ultrasound reconstruction," Genova, Italy, 2006.
[10] J. Xu, X. Yang, Q. Guo, and K. Sun, "Texture-based 3D ultrasound real-time volume rendering," *Jisuanji Gongcheng/Computer Engineering*, vol. 32, pp. 231-232, 2006.
[11] O. T. V. Ramm and S. W. Smith, "Real time volumetric ultrasound imaging system," *Journal of Digital Imaging*, vol. 3, pp. 261-266, 1990.
[12] B. J. Krenning, M. M. Voormolen, and J. R. T. C. Roelandt, "Assessment of left ventricular function by three-dimensional echocardiography," *Cardiovasc Ultrasound*, vol. 1(1), pp. online, 2003.
[13] J. C. Bamber and C. Daft, "Adaptive filtering for reduction of speckle in ultrasound pulse-echo images," *Ultrasonics*, pp. 41-44, 1986.
[14] J. C. Bamber and G. Cook-Martin, "Texture analysis and speckle reduction in medical echography," presented at Proceedings of SPIE, 1987.
[15] J. C. Bamber and J. V. Philips, "Real-time implementation of coherent speckle suppression in B-scan images," *Ultrasonics*, vol. 29, pp. 218-224, 1991.
[16] D. C. Crawford, D. S. Bell, and J. C. Bamber, "Implementation of ultrasound speckle filters for clinical trial," presented at Proceedings of IEEE Ultrasonic Symposium, 1990.
[17] D. C. Crawford, D. S. Bell, and J. C. Bamber, "Compensation for the signal processing characteristics of ultrasound B-mode scanners in adaptive speckle reduction," *Ultrasound in Medicine and Biology*, vol. 19, pp. 469-485, 1993.
[18] T. Loupas, W. N. Mcdicken, and P. L. Allan, "An adaptive weighted median filter for speckle suppression in medical ultrasonic images," *IEEE transactions on circuits and systems*, vol. 36, pp. 129-135, 1989.
[19] X. Hao, S. Gao, and X. Gao, "A novel multiscale nonlinear thresholding method for ultrasonic speckle suppressing," *IEEE Transactions on Medical Imaging*, vol. 18, pp. 787 - 794, 1999.
[20] X. Zong, A. F. Laine, and E. A. Geiser, "Speckle reduction and contrast enhancement of echocardiograms via multiscale nonlinear processing," *IEEE Transactions on Medical Imaging*, vol. 17, pp. 532-540, 1998.
[21] K. Z. Abd-Elmoniem, A.-B. M. Youssef, and Y. M. Kadah, "Real-time speckle reduction and coherence enhancement in ultrasound imaging via nonlinear anisotropic diffusion," *IEEE Transactions on Biomedical Engineering*, vol. 49, pp. 997-1014, 2002.
[22] E. D. Angelini, A. F. Laine, S. Takuma, J. W. Holmes, and S. Homma, "LV volume quantification via spatiotemporal analysis of real-time 3-D echocardiography," *IEEE Transactions on Medical Imaging*, vol. 20, pp. 457 - 469, 2001.
[23] Q. Duan, E. D. Angelini, and A. Laine, "Assessment of visual quality and spatial accuracy of fast anisotropic diffusion and scan conversion algorithms for real-time three-dimensional spherical ultrasound," presented at SPIE International Symposium Medical Imaging, San Diego, CA, USA, 2004.
[24] K. Z. Abd-Elmoniem, Yasser M. Kadah, and A.-B. M. Youssef, "Real time adaptive ultrasound speckle reduction and coherence," presented at Proceedings of 2000 International Conference on Image Processing, Vancouver, BC, Canada, 2000.
[25] Y. Yu and S. T. Acton, "Segmentation of ultrasound imagery using anisotropic diffusion," presented at Asilomar Conference on Signals, Systems and Computers, 2001.
[26] Y. Yu and S. T. Acton, "Speckle reducing anisotropic diffusion," *IEEE Transactions on Image Processing*, vol. 11, pp. 1260-1270, 2002.
[27] J. Montagnat, M. Sermesant, H. Delingette, and e. al, "Anisotropic filtering for model-based segmentation of 4D cylindrical echocardiographic images," *Pattern Recognition Letters*, vol. 24, pp. 815-828, 2003.
[28] P. Perona and J. Malik, "Scale space and edge detection using anisotropic diffusion," presented at IEEE Workshop on Computer Vision, 1987.
[29] P. Perona and J. Malik, "Scale-space and edge detection using anisotropic diffusion," *IEEE Trans Pattern Anal Machine Intell*, vol. 12, pp. 629-639, 1990.
[30] J. Weickert, B. M. t. H. Romeny, and M. A. Viergever, "Efficient and reliable schemes for nonlinear diffusion filtering," *IEEE Transactions on Image Processing*, vol. 7, pp. 398-410, 1998.
[31] S. Herz, C. Ingrassia, S. Homma, K. Costa, and J. Holmes, "Parameterization of left ventricular wall motion for detection of regional ischemia.," *Annals of Biomedical Engineering*, vol. 33, pp. 912-919, 2005.
[32] Q. Duan, E. D. Angelini, S. L. Herz, O. Gerard, P. Allain, C. M. Ingrassia, K. D. Costa, J. W. Holmes, S. Homma, and A. F. Laine, "Tracking of LV Endocardial Surface on Real-Time Three-Dimensional Ultrasound with Optical Flow," presented at Third International Conference on Functional Imaging and Modeling of the Heart 2005, Barcelona, Spain, 2005.
[33] S. Tsuruoka, M. Umehara, F. Kimura, T. Wakabayashi, Y. Miyake, and K. Sekioka, "Regional wall motion tracking system for high-frame rate ultrasound echocardiography," presented at Proceedings of the 1996 4th International Workshop on Advanced Motion Control, AMC'96. Part 1, Tsu, Jpn, 1996.

[34] I. Mikic, S. Krucinski, and J. D. Thomas, "Segmentation and tracking in echocardiographic sequences: active contours guided by optical flow estimates," *IEEE transactions on medical imaging*, vol. 17, pp. 274-284, 1998.
[35] D. Boukerroui, J. A. Noble, and M. Brady, "Velocity Estimation in Ultrasound Images: A Block Matching Approach," in *Lecture Notes in Computer Science*, 2732 ed, 2003, pp. 586-598.
[36] W. Yu, N. Lin, P. Yan, K. Purushothaman, A. Sinusas, K. Thiele, and J. S. Duncan, "Motion Analysis of 3D Ultrasound Texture Patterns," in *Lecture Notes in Computer Science*, 2674 ed, 2003, pp. 252-261.
[37] N. Paragios, "A level set approach for shape-driven segmentation and tracking of the left ventricle," *IEEE Transactions on Medical Imaging*, vol. 22, pp. 773-776, 2003.
[38] E. Bardinet, L. D. Cohen, and N. Ayache, "Tracking and motion analysis of the left ventricle with deformable superquadratics," *Medical Image Analysis*, vol. 1, pp. 129-149, 1996.
[39] V. Behar, D. Adam, P. Lysyansky, and Z. Friedman, "The combined effect of nonlinear filtration and window size on the accuracy of tissue displacement estimation using detected echo signals," *Ultrasonics*, vol. 41, pp. 743-753, 2004.
[40] J. Bang, T. Dahl, A. Bruinsma, J. H. Kaspersen, T. A. N. Hernes, and H. O. Myhre, "A new method for analysis of motion of carotid plaques from RF ultrasound images," *Ultrasound in Medicine and Biology*, vol. 29, pp. 967-976, 2003.
[41] S. I. Rabben, S. Bjaerum, V. Sorhus, and H. Torp, "Ultrasound-based vessel wall tracking: An auto-correlation technique with RF center frequency estimation," *Ultrasound in Medicine and Biology*, vol. 28, pp. 507-517, 2002.
[42] J. D'Hooge, P. Claus, B. Bijnens, J. Thoen, F. Van De Werf, P. Suetens, and G. R. Sutherland, "Deformation imaging by ultrasound for the assessment of regional myocardial function," presented at 2003 IEEE Ultrasonics Symposium,, Honolulu, HI, USA, 2003.
[43] E. E. Konofagou, W. Manning, K. Kissinger, and S. D. Solomon, "Myocardial elastography - Comparison to results using MR cardiac tagging," presented at 2003 IEEE Ultrasonics Symposium,, Honolulu, HI, United States, 2003.
[44] M. A. Gutierrez, L. Moura, C. P. Melo, and N. Alens, "Computing optical flow in cardiac images for 3D motion analysis," presented at Proceedings of the 1993 Conference on Computers in Cardiology, London, UK, 1993.
[45] I.-S. Shin, P. A. Kelly, K. F. Lee, and D. A. Tighe, "Left ventricular volume estimation from three-dimensional echocardiography," presented at Proceedings of SPIE, Medical Imaging 2004 - Ultrasonic Imaging and Signal Processing, San Diego, CA, United States, 2004.
[46] B. D. Lucas and T. Kanade, "An iterative image registration technique with an application to stereo vision," presented at International Joint Conference on Artificial Intelligence (IJCAI), 1981.
[47] B. K. P. Horn and B. G. Schunck, "Determing optical flow," *Artificial Intelligence*, vol. 17, pp. 185-203, 1981.
[48] H. Nagel, "Displacement vectors derived from second-order intensity variations in image sequences," *Computer Vision Graphics Image Processing*, vol. 21, pp. 85-117, 1983.
[49] P. Anandan, "A computational framework and an algorithm for the measurement of visual motion," *International journal of Computer Vision*, vol. 2, pp. 283-310, 1989.
[50] A. Singh, "An estimation-theoretic framework for image-flow computation," presented at International Conference on Computer Vision, 1990.
[51] J. L. Barron, D. Fleet, and S. Beauchemin, "Performance of optical flow techniques," *Int. Journal of Computer Vision*, vol. 12, pp. 43-77, 1994.
[52] Q. Duan, E. D. Angelini, S. L. Herz, C. M. Ingrassia, O. Gerard, K. D. Costa, J. W. Holmes, and A. F. Laine, "Evaluation of Optical Flow Algorithms for Tracking Endocardial Surfaces on Three-Dimensional Ultrasound Data," presented at SPIE International Symposium, Medical Imaging 2005, San Diego, CA, USA, 2005.
[53] C. M. Ingrassia, S. L. Herz, K. D. Costa, and J. W. Holmes, "Impact of Ischemic Region Size on Regional Wall Motion," presented at Proceedings of the 2003 Annual Fall Meeting of the Biomedical Engineering Society, 2003.
[54] E. D. Angelini, D. Hamming, S. Homma, J. Holmes, and A. Laine, "Comparison of segmentation methods for analysis of endocardial wall motion with real-time three-dimensional ultrasound," presented at Computers in Cardiology, Memphis TN, USA, 2002.
[55] S. Herz, T. Pulerwitz, K. Hirata, A. Laine, M. DiTullio, S. Homma, and J. Holmes, "Novel Technique for Quantitative Wall Motion Analysis Using Real-Time Three-Dimensional Echocardiography," presented at Proceedings of the 15th Annual Scientific Sessions of the American Society of Echocardiography, 2004.
[56] N. B. Schiller, H. Acquatella, T. A. Ports, D. Drew, J. Goerke, H. Ringertz, N. H. Silverman, B. Brundage, E. H. Botvinick, R. Boswell, E. Carlsson, and W. W. Parmley, "Left ventricular volume from paired biplane two-dimensional echocardiography," *Circulation*, vol. 60, pp. 547-555, 1979.
[57] E. D. Folland, A. F. Parisi, P. F. Moynihan, D. R. Jones, C. L. Feldman, and D. E. Tow, "Assessment of left ventricular ejection fraction and volumes by real-time, two-dimensional echocardiography. A comparison of cineangiographic and radionuclide techniques," *Circulation*, vol. 60, pp. 760-766, 1979.
[58] Q. Duan, E. Angelini, S. L. Herz, C. M. Ingrassia, O. Gerard, K. D. Costa, J. W. Holmes, S. Homma, and A. Laine, "Dynamic Cardiac Information From Optical Flow Using Four Dimensional Ultrasound," presented at 27th Annual International Conference IEEE Engineering in Medicine and Biology Society (EMBS), Shanghai, China, 2005.
[59] B. J. C. Baxter, "The Interpolation Theory of Radial Basis Functions," Cambridge University, 1992, pp. 1-142.
[60] J. D. Humphrey, *Cardiovascular solid mechanics : cells, tissues, and organs*. New York, USA: Springer, 2002.
[61] M. B. Buchalter, J. L. Weiss, W. J. Rogers, E. A. Zerhouni, M. L. Weisfeldt, R. Beyar, and E. Shapiro, "Noninvasive Quantification of Left Ventricular Rotational Deformation in Normal Humans Using Magnetic Resonance Imaging Myocardial Tagging," *Circulation*, vol. 81, pp. 1236-1244, 1990.
[62] Q. Duan, E. Angelini, O. Gerard, S. Homma, and A. Laine, "Comparing optical-flow based methods for quantification of myocardial deformations on RT3D ultrasound," presented at IEEE International Symposium on Biomedical Imaging (ISBI), 2006.
[63] L. K. Waldman, Y. C. Fung, and J. W. Covell, "Transmural myocardial deformation in the canine left ventricle. Normal in vivo three-dimensional finite strains," *Circ Res*, vol. 57, pp. 152-163, 1985.
[64] M. Nieminen, A. F. Parisi, J. E. O'Boyle, E. D. Folland, S. Khuri, and R. A. Kloner, "Serial evaluation of myocardial thickening and thinning in acute experimental infarction: identification and quantification using two-dimensinoal echocardiography," *Circulation*, vol. 66, pp. 174-180, 1982.

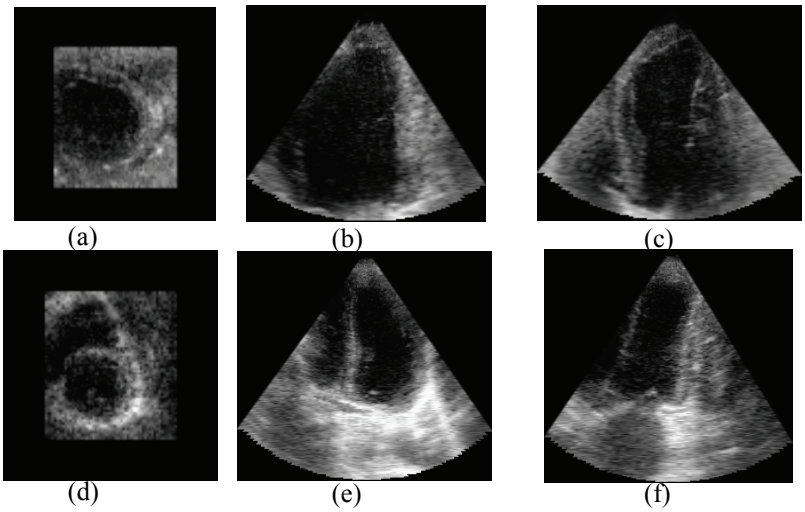

Figure 9.1 *Cross-sectional views at ED for (a-c) Open-chest dog data, prior to ischemia, (d-f) Patient with transplanted heart. (a, d) axial, (b, e) elevation and (c, f) azimuth views.*

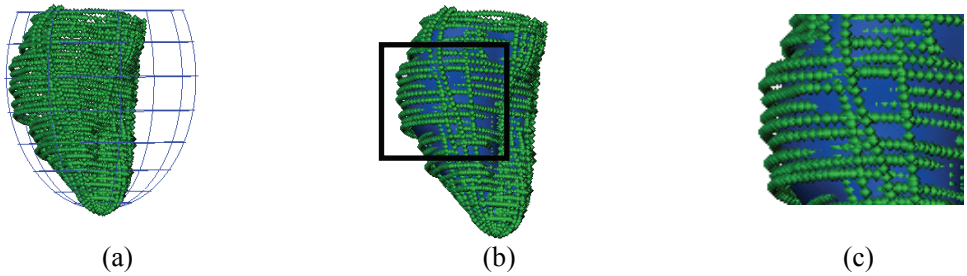

(a) (b) (c)

Figure 9.2 *Fitting process of the endocardial surface at ES. (a) Initial FEM mesh and data points. (b) Fitted FEM surface and data points. (c) Zoom on a small region with the FEM fitted surface and the data points.*

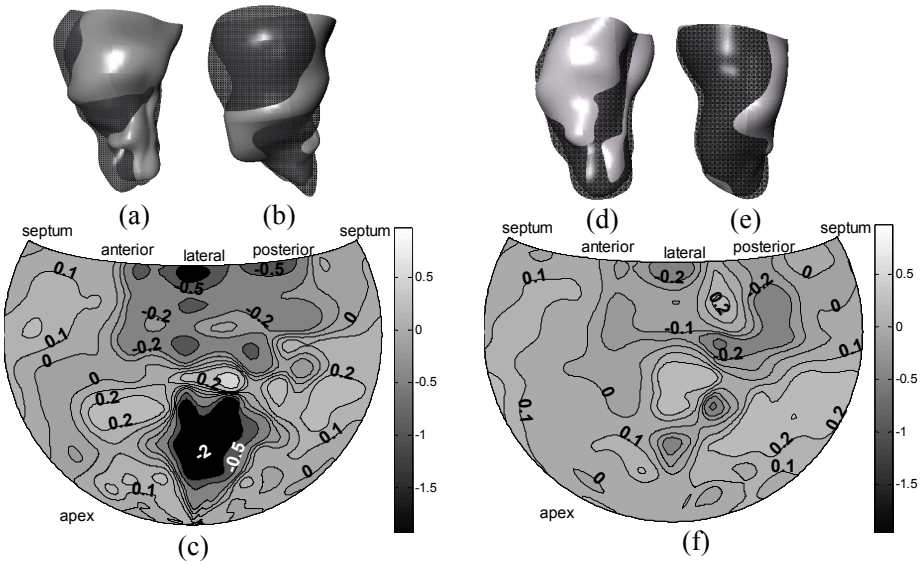

Figure 9.3 *Endocardial surfaces from open-chest dog data sets at ES. (a-c) Results on baseline data. (d-f) Results on post-ischemia data. Three-dimensional rendering of endocardial surfaces were generated from manual tracing (dark gray) and OF tracking (light gray) for (a, d) lateral views and (b, e) anterior views. (c, f) Relative difference maps between OF and manual tracing surfaces.*

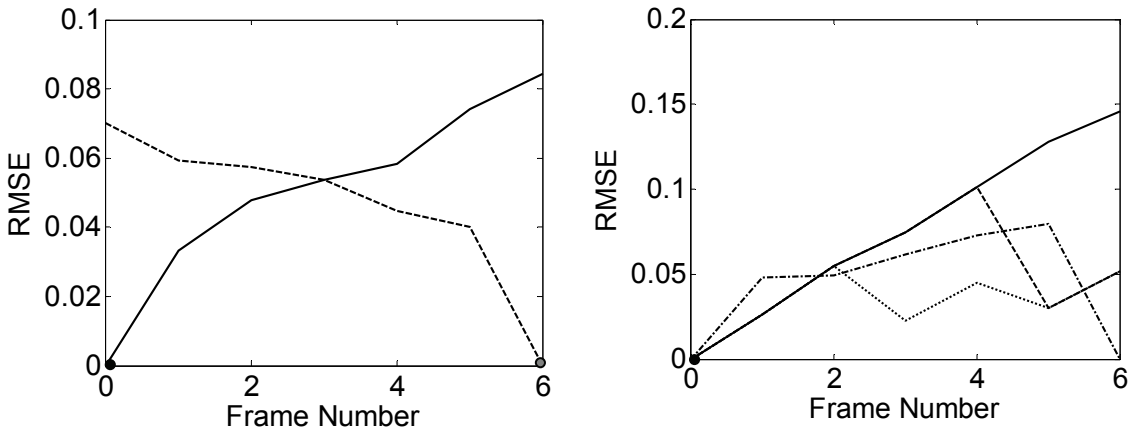

Figure 9.4 *Clinical Data: (a) RMSE between OF tracking and manual tracing: forward (solid line) and backward (dashed line). (b) RMSE between OF tracking and QLAB segmentation: forward tracking without re-initialization (solid line), forward tracking with re-initialization every fourth frame (dashed line), forward tracking with re-initialization every second frame (dotted line), and average result from forward and backward tracking without re-initialization (dashdot line).*

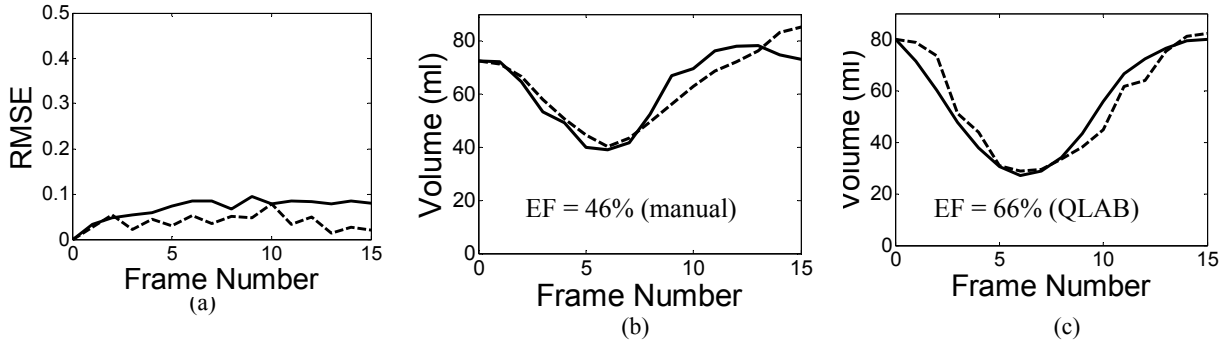

Figure 9.5 *Results on clinical data. (a) RMSE of radial difference for OF initialized with manual tracing (solid line) and QLAB segmentation with 2-frame re-initialization (dashed line); (b-c) LV volumes over one cardiac cycle: (b) Manual tracing (solid line) and OF initialized with manual tracing (dashed line); (c) QLAB segmentation (solid line) and OF initialized with QLAB segmentation (dashed line).*

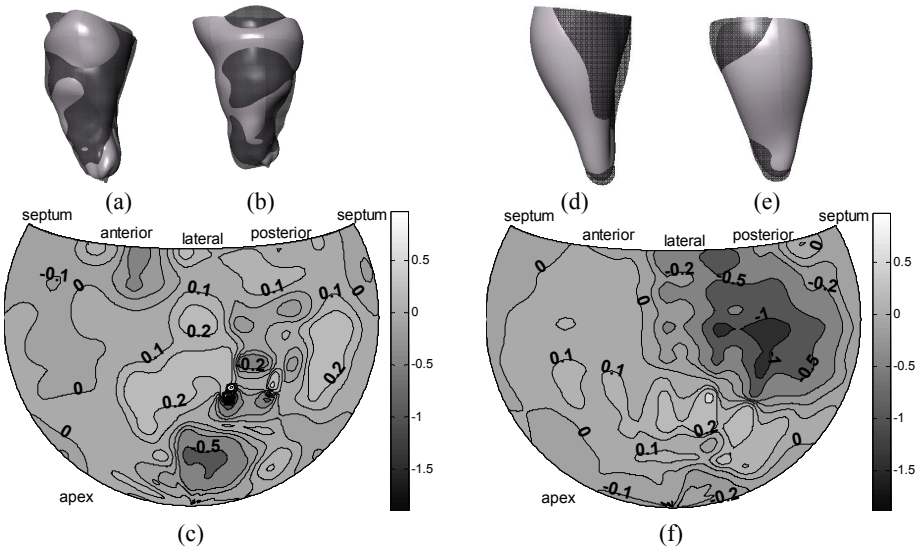

Figure 9.6 *Endocardial surfaces from clinical data at ES. (a-c) Manual tracing; (d-f) QLAB segmentation. Three-dimensional rendering of endocardial surfaces from segmentation method (dark gray) and OF tracking (light gray): (a, d) lateral view; (b, e) anterior view. Relative radial difference maps between OF tracking and the segmentation method.*

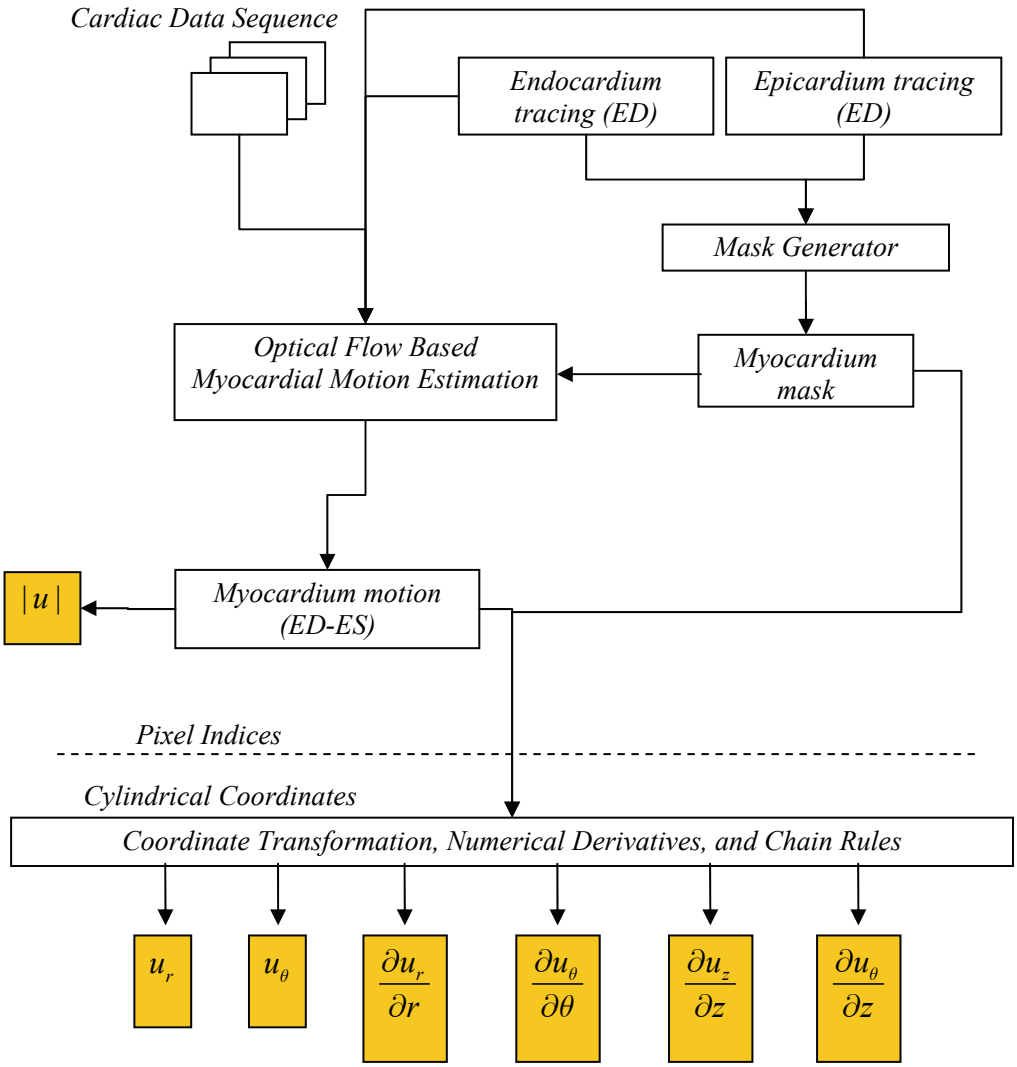

Figure 9.7 *Flowchart of the computational framework.*

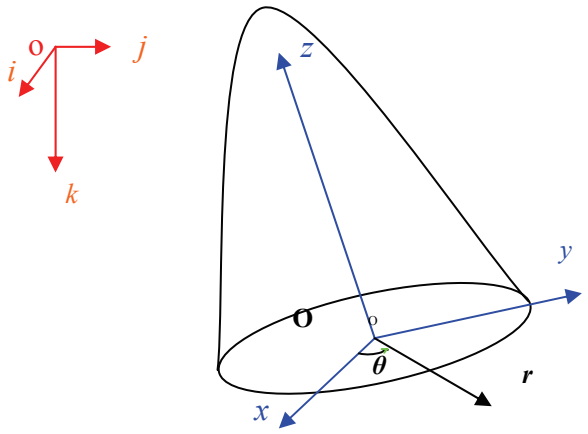

Figure 9.8 *Coordinate systems for data acquisition, and computation.*

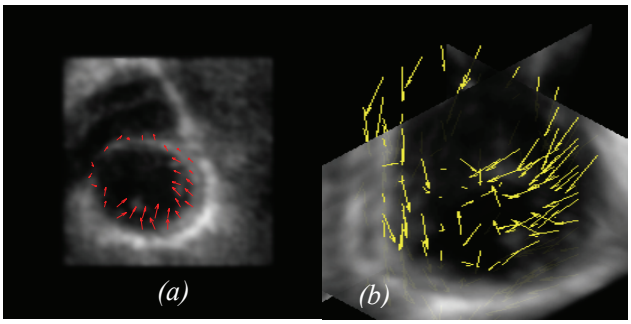

Figure 9.9 *Flow field: (a) 1 slice; (b) 3D rendering.*

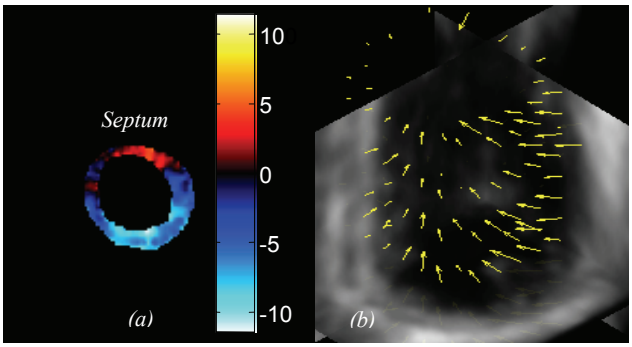

Figure 9.10 *Radial displacement: (a) 1 slice (blue: inward); (b) 3D rendering*

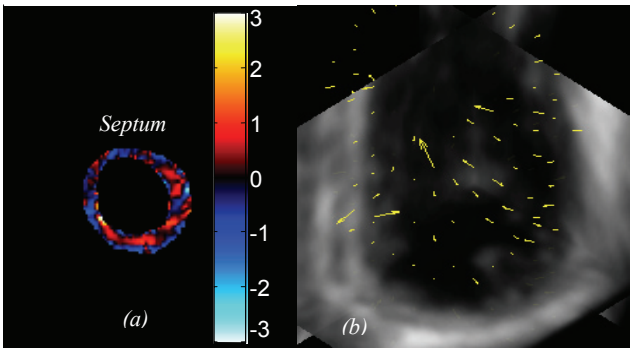

Figure 9.11 *Thickening: (a) 1 slice; (b) 3D rendering.*

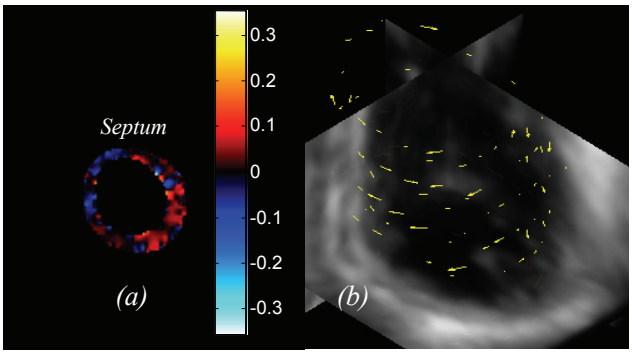

Figure 9.12 *Twist: (a) 1 slice (blue: clockwise); (b) 3D rendering*